Editors' Suggestion

Spin fluctuations sufficient to mediate superconductivity in nickelates

Paul Worm,[1] Qisi Wang,[2,3] Motoharu Kitatani,[4,5] Izabela Biało,[2,6] Qiang Gao,[7] Xiaolin Ren,[7] Jaewon Choi,[8] Diana Csontosová,[9] Ke-Jin Zhou,[8] Xingjiang Zhou,[7] Zhihai Zhu,[7] Liang Si,[10,1,*] Johan Chang,[2] Jan M. Tomczak,[11,1] and Karsten Held[1,†]

[1]*Institute of Solid State Physics, TU Wien, 1040 Vienna, Austria*
[2]*Physik-Institut, Universität Zürich, Winterthurerstrasse 190, CH-8057 Zürich, Switzerland*
[3]*Department of Physics, The Chinese University of Hong Kong, Shatin, Hong Kong, China*
[4]*Department of Material Science, University of Hyogo, Ako, Hyogo 678-1297, Japan*
[5]*RIKEN Center for Emergent Matter Sciences (CEMS), Wako, Saitama 351-0198, Japan*
[6]*AGH University of Krakow, Faculty of Physics and Applied Computer Science, 30-059 Krakow, Poland*
[7]*Beijing National Laboratory for Condensed Matter Physics, Institute of Physics, Chinese Academy of Sciences, Beijing 100190, China*
[8]*Diamond Light Source, Harwell Campus, Didcot OX11 0DE, United Kingdom*
[9]*Department of Condensed Matter Physics, Faculty of Science, Masaryk University, Kotlářská 2, 611 37 Brno, Czechia*
[10]*School of Physics, Northwest University, Xi'an 710127, China*
[11]*Department of Physics, King's College London, Strand, London WC2R 2LS, United Kingdom*

(Received 13 December 2023; revised 17 May 2024; accepted 20 May 2024; published 12 June 2024)

Infinite-layer nickelates show high-temperature superconductivity, and the experimental phase diagram agrees well with the one simulated within the dynamical vertex approximation (DΓA). Here, we compare the spin-fluctuation spectrum behind these calculations to resonant inelastic x-ray scattering experiments. The overall agreement is good. This independent cross validation of the strength of spin fluctuations strongly supports the scenario, advanced by DΓA, that spin fluctuations are the mediator of the superconductivity observed in nickelates.

DOI: 10.1103/PhysRevB.109.235126

I. INTRODUCTION

Contrasting cuprates [1] to the new nickelate superconductors [2–9] offers the unique opportunity to understand high-temperature (T_c) superconductivity more thoroughly: the two systems are similar enough to expect a common origin of superconductivity, but at the same time distinct enough to pose severe restrictions on any theoretical description. Structurally, both nickelate and cuprate superconductors consist of Ni(Cu)O_2 planes that host the superconductivity. These layers are separated by buffer layers of, e.g., Nd(Ca) atoms in the infinite-layer compound $NdNiO_2$($CaCuO_2$). Additionally, both Ni and Cu exhibit a nominal $3d^9$ electronic configuration in the respective parent compound, with a $3d_{x^2-y^2}$-derived band that is close to half filling.

Turning to the differences, a major one is that for cuprates the oxygen $2p$ bands, which strongly hybridize with the Cu $3d_{x^2-y^2}$ band, are below but close to the Fermi energy. This makes the parent compound a charge-transfer insulator [10], and the Emery model [11] the elemental model for cuprates. For nickelates, on the other hand, these $2p$ bands are shifted down relative to the $3d_{x^2-y^2}$ band which is fixed to the Fermi energy. As a consequence, the oxygen band is now sufficiently far away from the Fermi energy. While there is still the hybridization with the Ni $3d_{x^2-y^2}$ band, the oxygen $2p$ bands do not host holes if nickelates are doped. Instead, however, the rare-earth $5d$ bands are also shifted down (compared to the Ca bands that are above the Fermi energy in the cuprate $CaCuO_2$), now even cross the Fermi energy, and form two electron pockets around the Γ and A momentum points. This is evidenced by density functional theory (DFT) calculations [12–24] and, experimentally, by the negative Hall conductivity [2,4] for the infinite-layer compound. In all, this situation creates a seemingly more complicated multiband picture already for the undoped parent compound.

However, one of the pockets, the Γ pocket, shifts up and even above the Fermi energy either when (i) doping into the superconducting regime or (ii) when replacing Nd by La in DFT + dynamical mean-field theory (DMFT) calculations [25,26] (and $Ca_xLa_{1-x}NiO_2$ shows a very similar phase diagram to that of $Sr_xNd_{1-x}NiO_2$). Thus it appears unlikely that the Γ pocket is the key for superconductivity in nickelates. The A pocket, on the other hand, is more stable but it does not hybridize with the Ni $3d_{x^2-y^2}$ band [27]. Hence, in Ref. [25] the pockets were justifiably treated as a passive electron reservoir, largely decoupled from the Ni $3d_{x^2-y^2}$ band [28]. A similar picture has also been advocated in Refs. [29–31].

While the pockets are important for the (Hall) conductivity, we expect superconductivity to primarily emerge from the Ni $3d_{x^2-y^2}$ band which is strongly correlated. Indeed, calculations based on this single-band model, with appropriately calculated doping (to account for the pockets) [25],

*Corresponding author: siliang@nwu.edu.cn
†Corresponding author: held@ifp.tuwien.ac.at

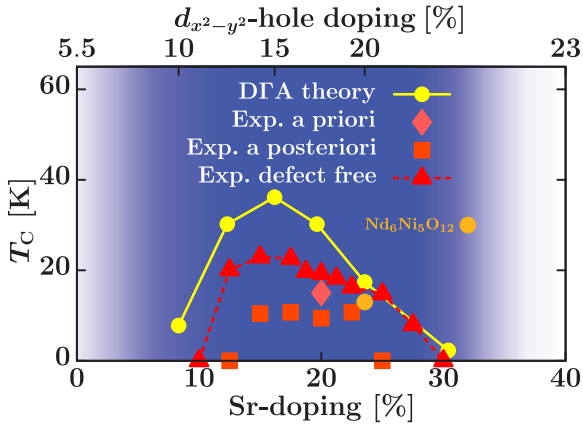

FIG. 1. Superconducting phase diagram, T_c vs Sr doping x, of $Sr_xNd_{1-x}NiO_2$. Following the discovery of nickelate superconductivity ("*a priori*," data taken from Ref. [2]), T_c was calculated ("DΓA theory," from Ref. [25]). The thus predicted T_c vs doping well agrees with the one measured "*a posteriori*" (from Ref. [3]), especially after "defect free" films have been synthesized (from Ref. [36]). Pentalayer $Nd_6Ni_5O_{12}$ [7] which has a 20% doping of the $d_{x^2-y^2}$ orbital [38] also agrees with theory and infinite-layer $Sr_xNd_{1-x}NiO_2$ at the same doping of the Ni $d_{x^2-y^2}$ orbital (upper x axis). The blue region indicates where only the Ni $d_{x^2-y^2}$ orbital and the A pocket cross the Fermi level in multiorbital DFT + DMFT.

using the dynamical vertex approximation (DΓA) [32–35] were able to compute the superconducting phase diagram, in good agreement with experiments [36,37]; see Fig. 1. In these DΓA calculations, antiferromagnetic (AFM) spin fluctuations mediate d-wave superconductivity. Despite the agreement of Fig. 1, it is imperative to further test this picture of spin-fluctuation-mediated superconductivity in nickelates. An important validation of the spin-fluctuation scenario comes from comparing the spin-wave spectrum predicted by DΓA to that measured in experiment. This is the aim of the present paper.

Specifically, signatures of AFM fluctuations have been measured in resonant inelastic x-ray scattering (RIXS) [39], nuclear magnetic resonance (NMR) [40], and muon spin rotation and relaxation (μSR) [41], where the fluctuation lifetime can exceed that of the muon [41]. Long-range AFM order is, however, absent in infinite-layer nickelates [42,43], a notable difference from cuprates. One natural explanation is the self-doping of the Ni $3d_{x^2-y^2}$ orbital induced by the A and Γ pockets. At hole-doping levels similar to that of the nickelate parent compounds, AFM order has also vanished in cuprates [44,45]. Consequently, electron doping (or changing a buffer layer to remove the pockets [46,47]) is presumably needed to stabilize AFM order in nickelates.

In the present paper, we calculate and analytically continue the magnetic susceptibility behind the DΓA calculation of Fig. 1. The nonlocal scattering amplitude (two-particle vertex) at the heart of this magnetic susceptibility directly enters the Cooper (particle-particle) channel as a pairing vertex and thus mediates superconductivity. For details see Ref. [35]. We also perform RIXS experiments and compare them to previous RIXS data by Lu *et al.* [39]. We find theory and experiment to be consistent. In particular, the strength of the experimental AFM coupling is similar to the one extracted from DΓA, advocating that it is sufficient to mediate the T_c observed in nickelate superconductors.

The outline of the paper is as follows: In Sec. II A, we describe the theory behind the modeling of spin fluctuations and superconductivity by a one-band Hubbard model, the *ab initio* calculated parameters used, and the DΓA calculations performed (cf. Appendix). Similarly, in Sec. II B the experimental methods are discussed, specifically the film growth and RIXS measurements. Section II C discusses possible shortcomings and sources of errors when extracting the paramagnon dispersion in theory and experiment. In Sec. III, we compare the theoretical and experimental magnetic spectrum. An analysis of the results in terms of a spin-wave model is presented in Sec. IV A. Its interaction dependence is elucidated in Sec. IV B, and two possible effects of disorder are discussed in Sec. IV C. Finally, Sec. V summarizes our results.

II. METHODS

A. Theory

1. Modeling

Previous work, based on DFT + DMFT [25,29], identified two bands that cross the Fermi surface in the superconducting regime of infinite-layer nickelates: one band with Ni $3d_{x^2-y^2}$ character and a pocket around the A momentum composed of Ni $3d$-t_{2g} + Nd $5d_{xy}$ character (subsequently referred to as the A pocket; for some dopings and rare-earth cations there is also an additional Γ pocket). However, the Ni $3d_{x^2-y^2}$ band and the A pocket within the same cell do not hybridize by symmetry. Hence, to a first approximation, they can be regarded as effectively decoupled. In this picture, superconductivity is expected to emerge from the Ni $3d_{x^2-y^2}$ band, which can be described by a one-band Hubbard model [48]:

$$\mathcal{H} = \sum_{ij\sigma} t_{ij} \hat{c}^\dagger_{i\sigma} \hat{c}_{j\sigma} + U \sum_i \hat{n}_{i\uparrow} \hat{n}_{i\downarrow}. \tag{1}$$

Here, t_{ij} denotes the hopping amplitude from site j to site i; $\hat{c}_i^\dagger$ ($\hat{c}_j$) are fermionic creation (annihilation) operators and σ marks the spin; $\hat{n}_{i\sigma} = \hat{c}^\dagger_{i\sigma} \hat{c}_{i\sigma}$ are occupation number operators. The Coulomb interaction is, because of screening, restricted to the on-site interaction U. The electrons taken away by the A pocket are accounted for by properly relating the Sr doping to the $d_{x^2-y^2}$ doping. This translation is displayed in the difference between lower and upper x axis of Fig. 1, which is based on multiorbital DFT + DMFT calculations [25].

2. Ab initio determined parameters

This Hubbard model has been used successfully as an effective low-energy model to calculate the superconducting dome in $NdNiO_2$ [25]. Here, we employ exactly the same *ab initio*–derived parameters for $NdNiO_2$; see Table I, where t is the nearest, t' the next-nearest, and t'' the next-next-nearest neighbor hopping amplitude. The tight-binding parameters are obtained after full relaxation of the lattice parameters with VASP [49] using the PBE [50] version of the generalized gradient approximation (GGA). In the presence of a substrate, we fix the in-plane lattice parameters to that of the substrate. For this crystal structure, the hopping parameters are subsequently

TABLE I. Hopping parameters of the effective Ni $3d_{x^2-y^2}$ orbital for nickelates with different spacer cations, two substrates [STO: $SrTiO_3$; LSAT: (La,Sr)(Al,Ta)O_3], and bulk.

System	t (eV)	t'/t	t''/t
$NdNiO_2$ (bulk)	0.395	−0.24	0.12
$NdNiO_2$/STO	0.377	−0.25	0.13
$NdNiO_2$/LSAT	0.392	−0.25	0.13
$LaNiO_2$ (bulk)	0.389	−0.25	0.12
$LaNiO_2$/STO	0.376	−0.23	0.11
$LaNiO_2$/LSAT	0.390	−0.22	0.11
$PrNiO_2$/STO	0.378	−0.25	0.13

obtained from a DFT calculation using Wien2K [51,52] and Wien2Wannier [53] to construct maximally localized Wannier orbitals [54]. As one can see from Table I the variation of these hopping parameters among different nickelates and substrates is minimal; cf. the discussion below. Because of this insensitivity to structural details we restrict ourselves in the following to one DΓA calculation resembling the hopping parameters of $NdNiO_2$ (bulk). Specifically, we use the same hopping parameters ($t = 0.395$ eV, $t'/t = -0.25$, $t''/t = 0.12$) as in Ref. [25] for calculating the data in Fig. 1 and use a temperature $T = 60$ K if not stated otherwise.

As in Ref. [25] the on-site Coulomb repulsion U is taken from constrained random phase approximation (cRPA) calculations. A natural first choice would be to simply use $U = U_{\mathrm{cRPA}}(\omega = 0)$, which is about 2.6 eV for the single-band approximation of $LaNiO_2$ [18]. However, a slightly enhanced static U is needed to empirically compensate for the neglected frequency dependence and increase of U above the effective plasma frequency. Further, previous studies [55–57] showed that cRPA overscreens the interaction. To take the above into account and in agreement with common practice, in Ref. [25] a slightly enhanced value of $U = 8t$ (3.11 eV) was considered as the best approximation. Further, we also use the same scheme to account for the self-doping effect of the A pocket as in Ref. [25]. That is, the doping of the one-band Hubbard model is determined from a 5 Ni-d and 5 Nd(La)-d DFT + DMFT calculation for $Sr_xNd(La)_{1-x}NiO_2$; see the Supplemental Material of Ref. [25]. Both here and in Ref. [25], the contribution of the pockets to superconductivity or the magnetic response, beyond an effective doping, has been neglected. This is justified since, due to its strong correlations, the $x^2 - y^2$ orbital dominates the magnetic susceptibility and (presumably) the pairing. Also note that the filling of the pockets is low.

3. Magnetic susceptibility

We compute the magnetic susceptibility χ_m in DΓA for the Hubbard model Eq. (1) using the parameters motivated in the last section. DΓA uses a DMFT solution as a starting point and introduces nonlocal correlations via the parquet or, in the simplified version used here, the Bethe-Salpeter equation [32,33,58]. We outline in the Appendix, for the sake of completeness, the steps necessary to obtain χ_m, and refer the reader to Ref. [34] for a more in-depth discussion of the DΓA, to Ref. [35] for details on how to calculate T_c, and to Ref. [59] for a first reading.

Let us stress that the λ-corrected DΓA susceptibility is very similar to the DMFT susceptibility. It is only corrected by a (**k**-independent) mass enhancement (λ correction), see Appendix, which physically corresponds to a reduction of the correlation length. This λ-corrected DΓA susceptibility yields good agreement with other numerical estimates [60] and also serves as a starting point for the subsequent calculation of the superconducting susceptibility or the eigenvalue. In contrast to the susceptibility and the spectrum, which can be very different in DΓA compared to DMFT despite the simple relation of their inverse through a constant λ (see Appendix), the dispersion (i.e., the maximum of the susceptibility as a function of **k** and ω) is the same for λ-corrected DΓA and DMFT. This can change in self-consistent DΓA [61],where spin fluctuations modify the self-energy which feeds back into the calculation of the susceptibility (instead of the λ-corrected mass enhancement). However, both approaches yield quite similar results for the antiferromagnetic susceptibility and the opening of the pseudogap [61].

4. Computational details of the DΓA calculation

The dynamical mean-field calculations (DMFT), which are used as the starting point for the dynamical vertex approximation (DΓA), are performed using the continuous-time quantum Monte Carlo method in its hybridization expansion (CT-HYB) implemented in w2DYNAMICS [62]. For all quantities, worm sampling [63] was used.

After DMFT convergence the two-particle Green's function of the corresponding Anderson impurity model (AIM) is obtained and from it the generalized DΓA susceptibility, as outlined in the Appendix. To obtain the physical susceptibility we need to sum the generalized susceptibility over two momenta and frequencies and perform the analytical continuation described in the next section. To ensure good statistics, we use order 10^9 measurements in a high statistic run for both one- and two-particle objects.

The DΓA calculations are performed using the DGApy [64] framework. A **k** mesh of at least (120,120,1) grid points is used, to ensure high-quality momentum resolution. We use about 60 (100) positive Matsubara frequencies in the vertex function for $T = 361$ K ($T = 60$ K). For the asymptotic treatment of the irreducible vertex, we use about 200 (500) additional frequencies in the shell region as described in Ref. [35]. The λ correction was performed both in the charge and the spin channel [33,65]; see the Appendix.

5. Analytic continuation

In the DΓA calculation, all quantities are defined in terms of imaginary time, or correspondingly, imaginary frequency (Matsubara frequency); see the Appendix. When comparing to experiments, however, results on the real axis are required. To obtain them we use the open-source package ana_cont [66], which employs the maximum entropy (maxent) method [67] for bosonic correlation functions like the physical susceptibility in Eq. (A7). Since the physical susceptibility $\chi_m^{q=\mathbf{q},\omega,\lambda}$ depends on momenta **q** and frequency ω, one analytic continuation of the frequency is performed for each

momentum. We fix all hyperparameters of the maxent routine by employing the "chi2kink" method [68] as implemented in ana_cont [66].

B. Experiment

1. Nickelate films

The precursor films of $Pr_{1-x}Sr_xNiO_3$ $(x = 0, 0.2)$ with 8 nm thickness were grown on (001)-oriented $SrTiO_3$ and $(LaAlO_3)_{0.3}(Sr_2TaAlO_6)_{0.7}$ (LSAT) substrates using pulsed laser deposition (PLD). Soft-chemistry reduction using CaH_2 powder was then performed to remove the apical oxygens of the precursor films. After reduction (300 °C, 100 min), the perovskite phase was transformed into an infinite-layer phase. The infinite-layer $Pr_{1-x}Sr_xNiO_2$ $(x = 0, 0.2)$ films were transferred to the PLD chamber to be deposited on their surfaces with 14-nm-thick $SrTiO_3$ protective top layers. The $Pr_{0.8}Sr_{0.2}NiO_2$ films grown on $SrTiO_3$ substrates are superconducting ones with the onset temperatures of superconducting transition ∼12 K.

2. RIXS experiments

Ni L_3-edge RIXS measurements were carried out at the I21 beamline at the Diamond Light Source. The energy resolution (monochromator and spectrometer combined) was set to 39 meV (full width at half maximum) at the Ni L_3 resonance (850.6 eV). Incident x rays with π polarization were used to enhance the paramagnon excitations. The scattering angle was fixed at 154° to maximize the in-plane momentum transfer. All RIXS spectra are collected at 16 K and normalized to the weight of the dd excitations.

C. Caveats

The DΓA calculation of the magnetic susceptibility is, as a matter of course, approximate. The DFT (GGA) starting point puts, e.g., the oxygen orbitals too close to the Fermi level. This is a bit less relevant for nickelates than for cuprates, and, in particular, when not including the oxygen orbitals in subsequent DMFT calculations (as done here). The next step, DMFT, is restricted to local correlations. Here, DMFT is used for translating the Sr doping to the doping of the Ni $3d_{x^2-y^2}$ orbital and for calculating a local vertex of the effective one-band Hubbard model. From this, we then calculate nonlocal spin fluctuations in DΓA through the Bethe-Salpeter ladder, and from these, in turn, the superconducting pairing glue is obtained. This procedure neglects how the superconducting fluctuations in the particle-particle channel feed back to the antiferromagnetic spin fluctuations in the particle-hole channel, and it also presumes that a local frequency-dependent vertex is a reasonably good starting point. Generally, this vertex is much more local than other properties such as the self-energy, even in the superconducting doping regime [34]. The good agreement of DΓA and diagrammatic quantum Monte Carlo simulations has been evidenced in Ref. [60].

Let us, here, mostly focus on two aspects that we believe are important to keep in mind when comparing the theoretical spectrum of the magnetic susceptibility to RIXS experiments: (i) The maxent approach is state-of-the-art to solve a *per se* ill-conditioned problem: analytically continuing imaginary-time data to real frequencies. Its error grows with frequency, since larger real frequencies only enter exponentially suppressed into the imaginary-time (or frequency) data. Further, maxent tends to broaden spectra [66]. This is especially true at large frequencies, where the maximum of the susceptibility becomes shallow. Altogether, this results in a rather large error bar of the overall dispersion.

(ii) On the experimental side, RIXS measurements do not probe magnetic excitations exclusively, but rather elementary excitations in general [69]. To extract the paramagnon dispersion, one fits several functions to the RIXS raw data. For example, the authors of Ref. [39] used a Gaussian for the elastic peak, a damped harmonic oscillator (DHO) for the magnon, an antisymmetrized Lorentzian for phonons, and the tail of an antisymmetrized Lorentzian for the high-energy background; see the supplementary information of Ref. [39]. Similarly, in our fitting function, a DHO convoluted with the energy resolution function is used to model the single magnon. The elastic peak is described with a Gaussian. The smoothly varying background is mimicked by a polynomial function. An additional Gaussian is included to describe the phonon mode at ∼70 meV when it becomes visible at a large in-plane momentum (>0.15 r.l.u.). For some dopings and momenta, we have a clear peak structure for the magnon and the error involved in this fitting is mild. In other situations, e.g., close to the X momentum, there is only a minor hump or shoulder, and the magnon energy is much more sensitive to the fitting procedure.

III. MAGNETIC RESPONSE IN NICKELATE SUPERCONDUCTORS

With the good agreement of the theoretical [35] and experimental phase diagrams [3,36] in Fig. 1, we here aim at analyzing whether the underlying magnetic fluctuations that mediate d-wave superconductivity in theory also agree with experiment. The magnetic spectrum and paramagnon dispersion for the two parent compounds $NdNiO_2$ and $PrNiO_2$ are shown in Figs. 2(b) and 2(c), respectively. Here, Fig. 2(a) displays the imaginary part of the magnetic susceptibility $\chi''_m(\omega, q)$ as computed in DΓA using a filling $n = 0.95$ of the Ni $3d_{x^2-y^2}$ orbital, originating from the self-doping due to the rare-earth pockets in $NdNiO_2$. For $PrNiO_2$ this self-doping is minimally smaller (3%). For the hopping parameters and Coulomb interaction, see Sec. II A 2. The dispersion is shown along the high-symmetry path in the Brillouin zone (BZ) from Γ to X to $M/2$ to Γ that is shown in the inset of Fig. 2(b). Let us emphasize once again that the DΓA dispersion, but not the spectrum, is the same as that of DMFT; see the Appendix. As for experiment, the data of Fig. 2(c) is our own measurement, and that of Fig. 2(b) was extracted from the RIXS measurements of Ref. [39] [70]. Given that we did not adjust any parameters [71], the agreement between theory and the magnon dispersion extracted from RIXS is quite good. This indicates that experimental spin fluctuations are similar to those leading to d-wave superconductivity in the DΓA calculations.

Looking more into the details, we see that the overall paramagnon bandwidth is systematically a bit larger in DΓA. For example, the peak of $\chi_m(q = X, \omega)$ is at $\omega_{peak} \sim 260$ meV in

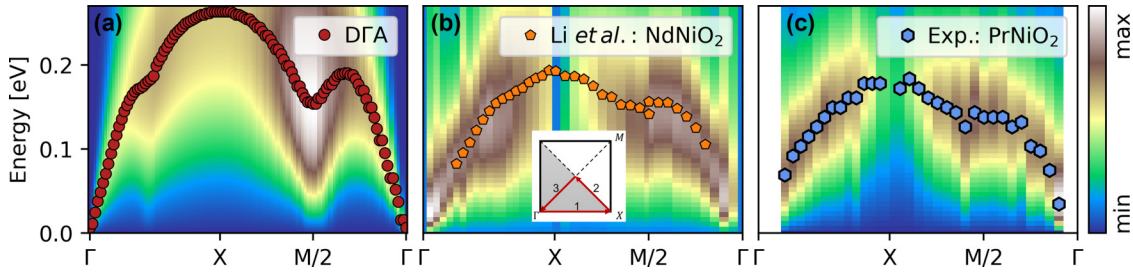

FIG. 2. Nickelate magnetic susceptibility (color map; arbitrary units) and paramagnon dispersion (symbols). (a) DΓA for $NdNiO_2$ at $T = 60$ K and $n = 0.95$ because of self-doping. (b) RIXS measurements for $NdNiO_2$ on STO at $T = 15$ K from Ref. [39]. (c) Our RIXS measurements for $PrNiO_2$ on STO at $T = 16$ K. Red, orange, and blue symbols mark the peak maximum. Inset in (b): Chosen k path through the Brillouin zone, where $\Gamma = (0, 0, 0)$, $X = (\pi, 0, 0)$, and $M/2 = (\pi/2, \pi/2, 0)$.

DΓA, while the measured one is close to ∼190 meV. While the tendency of the maximum entropy method to broaden spectra might also slightly affect the position of the maximum and the spectrum around the X point is more blurred in theory and experiment, overall the difference is beyond the maxent error. In agreement with the overall width, the slope of the linear dispersion around Γ deviates somewhat and hence we conclude: the overall width of the paramagnon dispersion in theory is noticeably larger than in experiment. This difference corresponds to a larger effective spin coupling J in DΓA, as we discuss in more detail in Sec. IV A.

Furthermore, the "dip" observed in the dispersion around the $M/2$ momentum, which corresponds to a next-next-nearest neighbor exchange J'' in a spin-wave picture, is more pronounced in theory than in experiment. In Sec. IV B, we show that using a larger $U = 9t$ (instead of $U = 8t$) results in a better agreement of the spin wave dispersion and also of the phase diagram of $Sr_xNd_{1-x}NiO_2$ on STO, which has considerably lower T_c's than $Sr_xNd_{1-x}NiO_2$ on LSAT. Please note that the origin for this experimental difference is not the minute change in lattice constant, but that growing $Sr_xNd_{1-x}NiO_2$ on LSAT results in cleaner films without stacking faults [36]. These "defect-free" films have a much lower resistivity and higher T_c's, and agree better with our best estimate $U = 8t$.

Let us now turn toward the doped compounds. DΓA results for $Sr_{0.2}Nd_{0.8}NiO_2$ with $x = 0.125$ (effective filling $n = 0.875$) and $x = 0.225$ ($n = 0.80$) are displayed in Figs. 3(a) and 3(b), respectively, and compared to the experimental dispersion (orange pentagons). Consistent with experiment, we observe a shift toward lower energies around the $M/2$ momentum. Furthermore, the amplitude of χ_m decreases as $q \to X$, which was also observed in Ref. [39] [72].

Similarly to the parent compound (Fig. 2), the bandwidth in DΓA is larger also at finite doping. Particularly the peak position at the X momentum shows a substantial deviation compared to the one extracted from RIXS. This may be partially (but not fully) attributed to the bias introduced both on the theoretical and experimental sides. On the one hand, we expect a worse performance of the numerical analytic continuation for large frequencies. A spectrum already relatively flat at the X momentum might be additionally broadened because of the maximum entropy analytic continuation. On the other hand, the intensity of the paramagnon peak is also reduced in RIXS [39], making the experimental fitting procedure more difficult. Notwithstanding, there is a larger theoretical dispersion (or J) than in experiment. Qualitatively similar, DΓA and RIXS show that the minimum at the $M/2$ momentum of the parent compounds turns into a flat dispersion or even a local maximum with doping.

IV. DISCUSSION

A. Effective spin-wave picture

In the limit of a large Hubbard interaction U, the Hubbard model [Eq. (1)] reduces to an effective Heisenberg Hamiltonian. We refer the reader to Ref. [73] and references therein for an extensive discussion for the one-orbital Hubbard model. While this mapping provides a direct relation between t, U, and the effective spin couplings J, the temperature does not enter, nor does the doping. Indeed, strictly speaking, the mapping onto the spin model is possible only for an insulator (at half filling). Yet, the parent compound Nd(Pr,La)NiO_2 is—in contrast to cuprates—neither half filled nor Mott insulating because of the finite pockets. Furthermore, the mapping onto a spin model becomes rather tedious in the presence of hoppings t' and t'' beyond nearest neighbors [73]. Nevertheless, the spin model and the spin-wave dispersion provide a somewhat

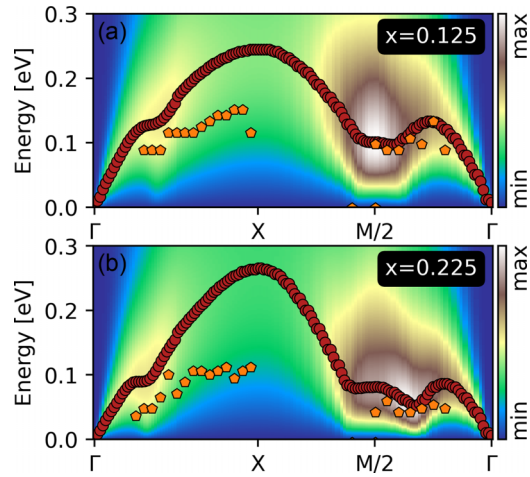

FIG. 3. Magnetic susceptibility of $Sr_xNd_{1-x}NiO_2$ for (a) $x = 0.125$ ($n = 0.875$) and (b) $x \simeq 0.225$ ($n = 0.8$) in DΓA. The red dots mark the maximum of the DΓA dispersion at each k point, while the orange pentagons are the corresponding RIXS peak locations from Ref. [39].

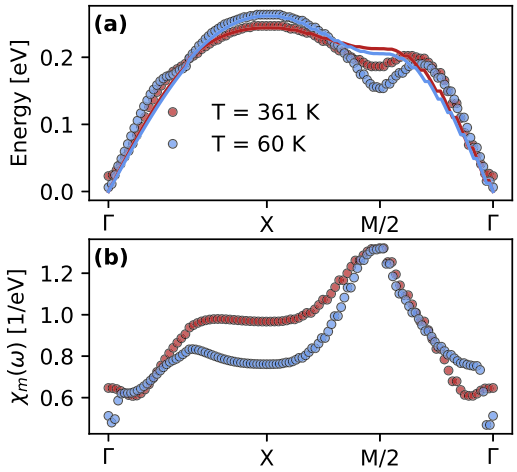

FIG. 4. Paramagnon dispersion obtained in DΓA for $LaNiO_2$ as a function of temperature. (a) DΓA dispersion (dots) and spin-wave fit (lines) using Eq. (2). (b) Magnetic DΓA susceptibility $\chi_m(\omega_{\text{peak}})$ at the peak frequency ω_{peak} of panel (a). Red: 361 K; blue: 60 K. Note that the DΓA dispersion but not the susceptibility is the same as that of DMFT.

intuitive picture for understanding the characteristics of spin fluctuations also in the present case of nickelates.

For these reasons, we employ here the same state-of-the-art approach as in experiment also for the DΓA data: that is, we fit the spin-wave dispersion of the Heisenberg model to our DΓA results in order to extract information about effective spin couplings J and J'. Including only the nearest neighbor (J) and next-nearest neighbor spin exchange J', the effective classical spin-wave dispersion for a spin-1/2 system is given by [73–75]

$$\omega_{\mathbf{k}} = Z_C\sqrt{\mathrm{A}_{\mathbf{k}}^2 - \mathrm{B}_{\mathbf{k}}^2}, \tag{2}$$

where Z_C is the spin-wave renormalization factor that accounts for the effects of quantum fluctuations and

$$\begin{aligned}\mathrm{A}_{\mathbf{k}} &= 2J + 2J'[\cos(k_x)\cos(k_y) - 1],\\ \mathrm{B}_{\mathbf{k}} &= J[\cos(k_x) + \cos(k_y)].\end{aligned} \tag{3}$$

To better compare with the values obtained in experiment, we fix $Z_C = 1.18$ as in Ref. [39]. Note that using Z_C is akin to rescaling (slightly reducing) the J and J' values. This way, the J and J' values extracted from the classical spin-wave theory are (slightly) better estimates for a spin-1/2 model (though one should mention that there is also some uncertainty in the numerical determination of Z_C). Figure 4 shows the thus obtained paramagnon dispersion and the corresponding value of the magnetic susceptibility $\chi_m(\omega_{\text{peak}})$.

To a first approximation (if $J' \ll J$), the width of the spin wave dispersion is $2J$ in Eq. (2), with $\omega_{\text{peak}\,\mathbf{k}} = \omega_{\text{peak}\,M/2} = 2J$. A finite J' adds a skewness to this as $\omega_{\text{peak}\,X} = 2J - 4J'$, whereas $\omega_{\text{peak}\,M/2} = 2J - 2J'$. The fact that the maximum of the dispersion is at $\mathbf{k} = X$ thus implies a ferromagnetic (negative) J'. This is qualitatively similar to cuprates which have, however, a considerably larger J (e.g., $J = 112$ meV and $J' = -15$ meV for La_2CuO_4 [74]). It is, on the other hand, different from other nickelates such as La_2NiO_4 [76] that show an antiferromagnetic (positive) J' and opposite skewness. This is because the latter require a multiband description with Ni $3d_{x^2-y^2}$ and Ni $3d_{z^2}$ orbital, resulting in a larger effective U [76].

TABLE II. Effective spin coupling J and J' for $NdNiO_2$ and $PrNiO_2$ obtained with DΓA (or DMFT) and measured in RIXS [39] given in units of meV. We list results for fits to DΓA dispersions at different interaction values $U = \{8, 9, 10\}$ in units of the hopping $t = 0.389$ eV and two different temperatures $T = \{300\text{ K}, 60\text{ K}\}$ for $U = 8t$, which is our best estimate on the basis of cRPA.

U (t)	8	8	9	10	RIXS $PrNiO_2$	RIXS $NdNiO_2$ [39]
T (K)	361	60	60	60	16	20
J (meV)	76	62	64	44	70.0 ± 5.5	63.6 ± 3.3
J' (meV)	–13	–23	–12	–12	-8.0 ± 3.8	-10.3 ± 2.3

The DΓA skewness is well described by the spin-wave fit, but there is a pronounced minimum at the $M/2$ point (for the parent compound) which is not well captured by the (J-J') spin-wave fit. We presume higher-order couplings, which are difficult to fit to the numerical DΓA data, are needed to account for such a minimum. Specifically, a next-next neighbor exchange J'' adds a term

$$\mathrm{A}_{\mathbf{k}} \to \mathrm{A}_{\mathbf{k}} - 2J''(1 - [\cos(2k_x) + \cos(2k_y)]/2) \tag{4}$$

in Eq. (2) [74]. For positive (antiferromagnetic) J'' this results in the observed local minimum at $M/2 = (\pi/2, \pi/2)$. The change of this minimum to a maximum, as observed with doping, then implies a change of sign of J''.

Similar to the cuprate superconductor La_2CuO_4 [74], we observe that the dispersion along the antiferromagnetic zone boundary becomes more pronounced as temperature is lowered. This mode hardening is mimicked by a *ferromagnetic* next-nearest spin coupling whose strength increases from $J' = -13$ meV at 361 K to $J' = -23$ meV at 60 K. For J the trend is opposite and its value gets reduced from 76 meV at 361 K to 62 meV at 60 K. Experimentally, $J = 63.6 \pm 3.3$ meV and $J' = -10.3 \pm 2.3$ meV at 20 K were reported in Ref. [39] for $NdNiO_2$. Similarly, we obtain $J = 70.0 \pm 5.5$ meV and $J' = -8.0 \pm 3.8$ meV at 16 K from RIXS for $PrNiO_2$; see Table II.

B. Interaction dependence

Table II suggests that the DΓA-fitted J value agrees better with experiment if a larger $U = 9t$ value is considered, instead of the cRPA estimate $U = 8t$ [77]. Figure 5 shows the magnetic susceptibility calculated in the same way as in Figs. 2 and 3, but now for $U = 9t$. The color maps in panels (a), (b), and (c) show $\chi_{\text{m}}^{q,\omega}$ along the same high-symmetry path as shown in the inset of Fig. 2(b). The red dots mark the maximum at each momentum, while the blue diamonds correspond to the peak maxima reported in RIXS [39].

Finally, Fig. 5(d) compares the peak location of the paramagnon dispersion for several interaction values. The overall width of the dispersion is reduced for larger U, as expected from the spin-wave picture discussed in the previous subsection. Subsequently, the agreement with experimental measurements is improved compared to the results of $U = 8t$

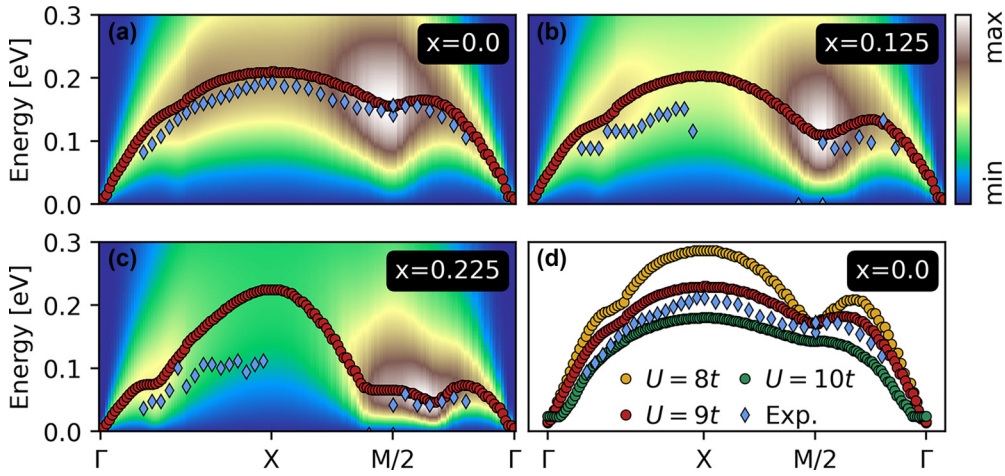

FIG. 5. Paramagnon spectrum of $Sr_xNd_{1-x}NiO_2$ using a larger interaction $U = 9t \simeq 3.5$ eV. (a) Parent compound $x = 0.0$ ($n = 0.95$) at $T \simeq 60$ K; (b) $x = 0.125$ ($n = 0.875$); (c) $x = 0.225$ ($n = 0.8$). The red dots mark the maximum of the dispersion at each k point, while the blue dots are the corresponding peak locations measured in RIXS (taken from Ref. [39]). (d) Paramagnon dispersion of the parent compound for different values of the interaction U.

in Figs. 2 and 3. Also, the superconducting phase diagram in Fig. 6 shows a better agreement between DΓA at $U = 9t$ (dark red) and $Sr_xNd_{1-x}NiO_2$ on STO. $Sr_xNd_{1-x}NiO_2$ on LSAT, on the other hand, better agrees with DΓA at the estimated $U = 8t$. This seemingly suggests that $U = 9t$ is more appropriate for nickelate films on STO. We think, however, that this agreement is by coincidence and that the larger $U = 9t$ value only mimics (in an imperfect way) the effect of disorder as discussed in the following.

The measurements for the same nickelate $NdNiO_2$ on different substrates, one on STO [3] (light blue) and one on LSAT [36] (dark blue), show about a factor of 2 difference in the superconducting T_c. The higher T_c for the LSAT substrate is, by the authors of Ref. [36], attributed to the difference in film cleanliness, with fewer lattice defects observed for the LSAT substrate. This conclusion is supported by scanning tunneling microscopy that shows fewer Ruddlesden-Popper

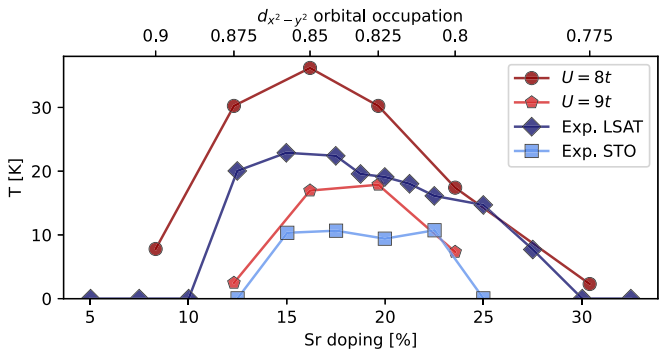

FIG. 6. Superconducting phase diagram T_c as a function of Sr doping for $Sr_xNd_{1-x}NiO_2$, comparing DΓA with $U = 8t$ ($U = 9t$) from Ref. [25] to experiment on a LSAT (STO) substrate from Ref. [36] (Ref. [3]). The increase of T_c in DΓA when using LSAT instead of STO in-plane lattice parameters is much weaker; the difference between the two substrates hence most likely reflects the improvement thanks to cleaner, defect-free films for the LSAT substrate.

stacking faults. Further support comes from a strongly reduced resistivity (by up to a factor of 3) for the samples grown on LSAT. Such a large difference cannot be explained by the minor differences of substrate strain [78].

On the theoretical side, we observe a similar difference in transition temperature between calculations using $U = 8t$ and $U = 9t$, respectively. However, the respective Wannier tight-binding parameters for $LaNiO_2$ [79] with in-plane lattice constants fixed to those of STO and LSAT are quite similar; see Sec. II A 2. That is, we find that the nearest neighbor hopping t increases by about ∼4% from STO to LSAT, while the ratios of t'/t and t''/t remain essentially the same. An increase of t is not surprising as the smaller in-plane lattice constant of LSAT increases the orbital overlap. On the other hand, the Hubbard interaction ($U_{\mathrm{cRPA}} = 2.6$ eV) essentially does not change when performing constrained random phase approximation calculations for $LaNiO_2$ with the a-b lattice parameters fixed to either that corresponding to LSAT or that of STO, respectively.

Considering these changes of the effective single-band Hamiltonian, we expect samples grown on LSAT to have an intrinsically larger T_c, since t sets the energy scale and a smaller U/t is also beneficial [25]. That being said, the expected difference in T_c, as a result of the slightly different intrinsic models, is closer to 10%–15% [80], but almost certainly not a factor of 2 [81]. For this reason we conclude that changes in our effective single-band Hubbard model do not explain differences in the measured T_c's for different substrates. The difference has to lie somewhere else, and the reduced number of defects when growing nickelates on LSAT is the most likely explanation for the enhanced T_c and reduced resistivity, as also originally suggested in Ref. [36].

Following this argument, the appropriate Hubbard interaction for the effective single-band description of infinite-layer nickelates should be close to our best estimate $U = 8t$ with an intrinsic $T_c^{\max} \simeq 30$ K, comparable to that measured on LSAT [82]. Consequently, we would expect the T_c of samples grown on STO to be similar (within 4%) once samples of comparable quality are synthesized. What remains to be

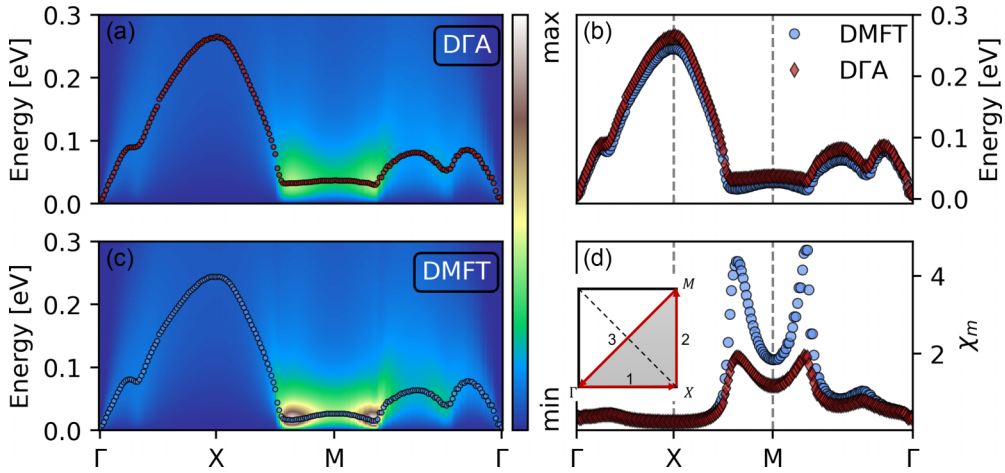

FIG. 7. Magnetic susceptibility of $Sr_xNd_{1-x}NiO_2$ for $x \sim 0.225$ ($n = 0.8$) within the effective single-orbital Hubbard model scenario. Color map of $\chi_m^{q,\omega}$ calculated by (a) DΓA and (c) DMFT. (b) Comparison of the maximum of the dispersion corresponding to the lines on top of the color maps in (a) and (c), respectively. (d) Peak value of the magnetic susceptibility; inset: k path in the BZ. The difference between DMFT and DΓA is the reduced correlation length; the dispersion in (b) is the same up to the numerical accuracy; see the Appendix. Parameters: $t = 0.389$ eV, $t'/t = -0.25$, $t''/t = 0.12$, $U = 8t$, $T = 60$ K.

understood is how defects and lattice disorder influence the paramagnon dispersion and T_c.

C. Effect of disorder and stacking faults on the paramagnon dispersions

To fully address the influence of impurities and lattice defects on the paramagnon dispersion, large-scale calculations for supercells that include these defects would be required. Such calculations are not feasible at the moment, at least not for DΓA calculations or similar many-body methods that include nonlocal fluctuations. For this reason, we will restrict ourselves here instead to qualitative considerations.

One possibility is that defects reduce the effective antiferromagnetic coupling strength J and, with reduced antiferromagnetic fluctuations, also T_c. While estimating the absolute influence of such local defects in RIXS is very difficult, if not impossible, samples that show a different T_c can be compared. Such a study would include measurements of several samples of the same "species," e.g., $Sr_{0.2}Nd_{0.8}NiO_2$ on STO, which show a sample-to-sample variation in T_c. Along the same lines, comparing the paramagnon dispersions for samples grown on different substrates (e.g., STO and LSAT) would yield valuable information about the connection between the paramagnon dispersion and T_c. A study similar to the latter has already been performed for the related $PrNiO_2$ compound [83]. The measurements suggest that the paramagnon dispersion and J are similar for samples grown on LSAT and STO. However, those measurements were done on the nonsuperconducting parent compound. Hence, it would be interesting to check whether the reported results remain unchanged if samples with different T_c's are measured directly. Let us, in this context, mention that for cuprates it was possible to correlate the increase of T_c with the increase of J for different cuprates [84]. Along this line of thinking, the better agreement of T_c and the RIXS spectrum of $NdNiO_2$ on STO for the larger $U = 9t$ might just mimic the suppression of J induced by disorder which is not included in our calculations. It does not mean that $U = 9t$ is the appropriate choice of interaction for these defect-full samples, but only that it gives (for the wrong reasons) similar effects as disorder for RIXS and T_c.

Let us also point out another way that lattice defects might influence T_c: decreasing the magnetic correlation length ξ. Particularly, if stacking faults and similar defects introduce artificial "grain boundaries" [85], ξ might be restricted to stay below the typical grain-boundary distance, without directly changing the effective antiferromagnetic coupling strength J. Though conceptually somewhat different, the λ correction in DΓA [33] has a similar effect in the sense that λ causes a decrease in the magnetic correlation length. Such a reduced correlation length (added mass), however, essentially does not change the paramagnon dispersion; see Fig. 7 and the discussion in the next paragraphs. Furthermore, the intensity primarily changes around the $M = (\pi, \pi)$ momentum, where the susceptibility and ξ are the largest.

Such an effective paramagnon-mass enhancement or reduced ξ is difficult to extract from RIXS, which cannot access the M point in nickelates. Yet, it is precisely the strength of the susceptibility around the M momentum, which, from a spin-fluctuation or DΓA perspective, is most important for T_c. The M point and a prospective difference in correlation length ξ for different substrates might be accessible in neutron scattering. If measurements of the magnetic correlation length ξ for superconducting samples grown on different substrates show a suppressed ξ at the M point for samples grown on STO compared to those grown on LSAT, this would support this second disorder scenario.

To investigate the influence of a suppressed correlation length, we compare χ_m between DMFT and DΓA in Fig. 7 along a high-symmetry path through the BZ now including the M momentum [see inset in panel (d) for the Brillouin zone]. We choose the overdoped compound ($x = 0.225$) since DMFT shows no antiferromagnetic order for this doping. Hence, we can directly compare χ_m between DMFT (no λ correction) and DΓA (with the λ correction determined to be

$\lambda = 0.105$); cf. Ref. [34] and the Appendix for the close relation of both susceptibilities. The DMFT susceptibility with a large correlation length ξ, especially around $\mathbf{q} = (\pi, \pi)$, is shown in panel (c), while DΓA with a correlation length ξ reduced by λ (see Appendix) is displayed in panel (a).

We draw the location of the peak in χ_{m} at each momentum in Fig. 7(b). It remains essentially unchanged in the presence of a DΓA λ correction, i.e., with a reduced ξ. The magnitude of the respective susceptibility at the peak is, however, drastically different around the M momentum, as can be seen in Fig. 7(d). A suppression of χ_m is strongest when the DMFT susceptibility is large, which is no surprise since $\chi_m \to 1/(1/\chi_m + \lambda)$ in DΓA. Hence, a reduction of the correlation length for antiferromagnetic fluctuations is expected to be virtually invisible in RIXS measurements, which do not access the M point. At the same time, the reduction of T_c can be dramatic.

Let us further note that we observe incommensurate antiferromagnetic fluctuations, evidenced by the shift of the maximum amplitude slightly away from M in Fig. 7(d). This is typical for overdoped cuprates [86,87] [88]. For nickelates, measurements that could distinguish commensurate from incommensurate spin fluctuations have, to the best of our knowledge, not been performed yet.

V. CONCLUSION

The pairing symmetry obtained in DΓA for nickelates is d wave, reminiscent of that in cuprates [45]. On the experimental side, the pairing symmetry of nickelates remains an open question as results are still inconclusive [89–91]. Also the mechanism for superconductivity remains highly controversial, not only for nickelates but also for cuprates. Many different mechanisms have been proposed [45,92–94]. In DΓA spin fluctuations mediate superconductivity [95].

Further, in the case of nickelates, even the minimal model is hotly debated. Among others, the relevance of multiorbital physics [21,96,97], Kondo physics [98], or even phonons [99] has been suggested. The single-band Hubbard model with an appropriately calculated doping of the Ni $3d_{x^2-y^2}$ orbital, which was used in the present paper, is arguably the simplest possible model for spin fluctuations and superconductivity in nickelates. It correctly reproduces the doping range of superconductivity, the absolute value of T_c, and also the skewness of the phase diagram. Here, the skewness is a consequence of the largely decoupled ligand pockets which accommodate part of the holes from the Sr doping in a nonlinear fashion. This skewness of the superconducting dome is a notable difference to cuprates.

Given the good agreement of the superconducting phase diagram and antiferromagnetic fluctuations at its origin, a critical check of whether or not spin fluctuations with similar characteristics are observed in experiment is imperative. To achieve this validation, we compared the paramagnon dispersion calculated in DΓA with the one extracted from RIXS, both from our measurements and those from Ref. [39]. Note that the λ-corrected DΓA susceptibility only differs from the DMFT one around the (incommensurate) antiferromagnetic wave vector (see Fig. 7).

We find the spin spectrum is overall similar, especially when considering biases expected both from theory and experiment. This means that the experimental spin fluctuations are consistent with the observed T_c in nickelates within the spin-fluctuation scenario of superconductivity. Then, the weaker spin fluctuations (or J) in nickelates, compared to cuprates, might also explain their lower T_c.

The agreement is however not perfect. The total width of the paramagnon dispersion (or J) is somewhat smaller in experiment than in theory. Using an enhanced Coulomb interaction $U = 9t$ in DΓA (instead of $U = 8t$ estimated from cRPA) matches better the RIXS spectrum and also the superconducting phase diagram of $Sr_xPr_{1-x}NiO_2$ and $Sr_xNd_{1-x}NiO_2$ on an STO substrate. However, these films are defect-full, and in our view the larger $U = 9t$ is not physically correct but rather an imperfect way to mimic the effect of defects. This is supported by the fact that substantially larger T_c's are observed for defect-free $Sr_xNd_{1-x}NiO_2$ on a LSAT substrate in excellent agreement with the DΓA using the proper $U = 8t$ estimate. [Note that the difference of LSAT and STO in-plane lattice constants and thus also the DΓA hopping parameters are way too small to explain the (by a factor of 2) higher T_c and (by a factor of 3) lower resistivity.]

As discussed in Sec. IV C local disorder can reduce J. From this perspective, $Sr_xNd_{1-x}NiO_2$ on STO with more disorder should indeed show a larger J and a smaller dispersion in RIXS, imperfectly mimicked by a larger U. If the disorder is rather cutting off the spin correlation length—and Ruddlesden-Popper stacking faults might do that—we show that the effect on the RIXS dispersion can be negligible. In this scenario, disorder only affects the peak height at $M = (\pi, \pi)$, which is not accessible in RIXS but in neutron scattering experiments. In this "cutting off the correlation length" scenario, the difference between RIXS and theory at the proper $U = 8t$ must be of another origin.

In all, we believe that our joint theoretical and experimental investigation strengthens the case for spin-fluctuation mediated superconductivity in nickelates.

Let us close by comparing nickelates to cuprates, both of which are commonly modeled through a Hubbard model. The main difference is that in the nickelates there are additional electron pockets; in the cuprates holes from doping go predominately into the oxygen p orbitals instead of the Cu $3d_{x^2-y^2}$ orbital. These in turn hybridize with the Cu $3d_{x^2-y^2}$ orbital and form a single band that crosses the Fermi energy, which, with some caveats [100], can be described by a Hubbard model. This common physics reflects in similar magnetic excitations as measured by RIXS. The main difference is a quantitatively smaller width of the magnetic RIXS dispersion, concomitant with a smaller exchange J and a lower T_c for nickelates.

Note added. Most recent angular-resolved photoemission spectroscopy (ARPES) experiments [101,102] strongly support the one $3d_{x^2-y^2}$-orbital plus A-pocket scenario employed in our calculations on the basis of DFT + DMFT: There is no Γ pocket for superconducting $Sr_{0.2}La_{0.8}NiO_2$, nor are there additional $3d_{z^2}$ bands at the Fermi level as advocated in other scenarios [21,96,97,103]. Also, the mass renormalization factor of about 3 agrees with our theoretical description at the cRPA estimated $U = 8t$ (see Supplemental Fig. 3 of Ref. [25]).

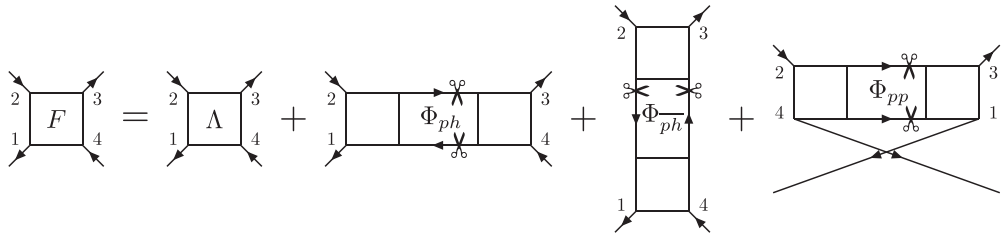

FIG. 8. Parquet decomposition of the full vertex function F into its components based on the two-particle reducibility. Λ is the fully irreducible vertex, and ϕ_r with $r = \{\text{ph}, \overline{\text{ph}}, \text{pp}\}$ is the reducible part of F in the particle-hole (ph), particle-hole transversal ($\overline{\text{ph}}$), and particle-particle (pp) channel.

ACKNOWLEDGMENTS

We thank Simone Di Cataldo, Oleg Janson, and Jan Kuneš for helpful discussions. We further acknowledge funding through the Austrian Science Funds (FWF) Projects I 5398, I 6142, P 36213, SFB Q-M&S (FWF Project ID F86), the Swiss National Science Foundation under Grant No. 200021_188564, Grant-in-Aids for Scientific Research (JSPS KAKENHI) Grants No. JP21K13887 and No. JP23H03817, the Research Grants Council of Hong Kong (ECS No. 24306223), and Research Unit QUAST by the Deutsche Foschungsgemeinschaft (DFG; Project ID FOR5249) and FWF (Project ID I 5868). L.S. is thankful for the starting funds from Northwest University. I.B. acknowledges support from the Swiss Government Excellence Scholarship under Project No. ESKAS-Nr: 2022.0001. The work at IOP (Q.G., X.R., X.J.Z., and Z.H.Z.) was supported by the National Natural Science Foundation of China under Grant No. 12074411. Calculations have been done in part on the Vienna Scientific Cluster (VSC).

APPENDIX: MAGNETIC SUSCEPTIBILITY IN DΓA

As a first step to calculate the magnetic susceptibility χ_m, we solve the Hubbard model Eq. (1) within DMFT and subsequently sample the local two-particle Green's function ($G^{(2)}$) for the corresponding Anderson impurity model (AIM):

$$G^{(2)\nu_1\nu_2\nu_3\nu_4} = \int_0^\beta \int_0^\beta \int_0^\beta \int_0^\beta d\tau_1 d\tau_2 d\tau_3 d\tau_4 G^{(2)}(\tau_1, \tau_2, \tau_3, \tau_4) e^{i\nu_1\tau_1} e^{-i\nu_2\tau_2} e^{i\nu_3\tau_3} e^{-i\nu_4\tau_4}, \tag{A1}$$

where the two-particle Green's function in terms of imaginary time (τ) is defined as

$$G^{(2)}_{1234}(\tau_1, \tau_2, \tau_3, \tau_4) \equiv \langle \mathcal{T}[\hat{c}_1(\tau_1)\hat{c}_2^\dagger(\tau_2)\hat{c}_3(\tau_3)\hat{c}_4^\dagger(\tau_4)]\rangle. \tag{A2}$$

Since our Hamiltonian Eq. (1) does not explicitly depend on time, one frequency can be removed by using energy conservation. If not stated otherwise we will use the particle-hole (ph) notation:

ph-notation:	pp-notation:
$\nu_1 = \nu$	$\nu_1 = \nu$
$\nu_2 = \nu - \omega$	$\nu_2 = \omega - \nu'$
$\nu_3 = \nu' - \omega$	$\nu_3 = \omega - \nu$
$\nu_4 = \nu'$	$\nu_4 = \nu'$

The two-particle Green's function in Eq. (A1) can thus be written in terms of three instead of four frequencies. Further, it can be expressed in terms of disconnected (free) and connected (vertex) parts:

$$G^{(2),\omega\nu\nu'}_{\sigma\sigma'} = \delta_{\omega 0} G^\nu_\sigma G^{\nu'}_{\sigma'} - \delta_{\nu\nu'}\delta_{\sigma\sigma'} G^\nu_\sigma G^{\nu-\omega}_{\sigma'} + \frac{1}{\beta} G^\nu_\sigma G^{\nu-\omega}_\sigma F^{\omega\nu\nu'}_{\sigma\sigma'} G^{\nu'-\omega}_{\sigma'} G^{\nu'}_{\sigma'}, \tag{A3}$$

where F is the so-called vertex function which encodes all scattering events on the two-particle level and $G^\nu = -\int_0^\beta \int_0^\beta d\tau_1 d\tau_2 \, \langle \mathcal{T} c_1(\tau_1) c^\dagger(\tau_2)\rangle e^{i\nu(\tau_1-\tau_2)}$ is the one-particle Green's function. All diagrams contained in the vertex function F can be classified unambiguously by the parquet decomposition,

$$F^{\omega\nu\nu'}_{\sigma\sigma'} = \Lambda^{\omega\nu\nu'} + \Phi^{\omega\nu\nu'}_{\text{pp},\sigma\sigma'} + \Phi^{\omega\nu\nu'}_{\overline{\text{ph}},\sigma\sigma'} + \Phi^{\omega\nu\nu'}_{\text{ph},\sigma\sigma'}, \tag{A4}$$

based on their two-particle reducibility, i.e., whether or not a diagram decomposes if one "cuts" two one-particle Green's function lines. For a diagrammatic depiction and the definition of Λ and Φ_r see Fig. 8.

We now also define the irreducible vertices $\Gamma_r = F - \Phi_r$, where $r = \{\text{ph}, \overline{\text{ph}}, \text{pp}\}$ is either one of the three scattering channels. Furthermore, we assume SU(2) symmetry, i.e., restrict ourselves to the paramagnetic phase. This spin symmetry leads to only two independent spin combinations $F_m = F_{\uparrow\uparrow} - F_{\uparrow\downarrow}$ (magnetic) and $F_d = F_{\uparrow\uparrow} + F_{\uparrow\downarrow}$ (density) [34]. The vertex F can also be expressed directly in terms of any irreducible vertex via the respective Bethe-Salpeter equation (BSE):

$$F^{\omega\nu\nu'}_{d/m} = \Gamma^{\omega\nu\nu'}_{d/m,\text{ph}} + \frac{1}{\beta}\sum_{\nu_1} \Gamma^{\omega\nu\nu'}_{d/m,\text{ph}} G^{\nu_1} G^{\nu_1-\omega} F^{\omega\nu\nu'}_{d/m}. \tag{A5}$$

Here, we have written the BSE only for Γ_{ph}, and we use the inverse of Eq. (A5) to extract the local Γ_{ph}. To obtain a q-dependent susceptibility we use a BSE-like equation for the

generalized, now momentum-**k** dependent susceptibility:

$$\chi_{d/m}^{qkk'} = \chi_0^{qkk'} - \chi_0^{qkk} \frac{1}{\beta^2} \sum_{k_1} \Gamma_{d/m}^{qkk_1} \chi_{d/m}^{qk_1k'}. \tag{A6}$$

Here $k = (\mathbf{k}, \nu)$ and $q = (\mathbf{q}, \omega)$ are fermionic and bosonic four-point vectors in generalization of local, frequency-only-dependent quantities of the AIM. Further, we approximate $\Gamma_{d/m}^{qkk_1} = \Gamma_{d/m}^{\omega\nu\nu'}$, i.e., the respective irreducible DMFT vertex. The physical susceptibility is finally obtained by summing over kk', i.e., $\chi_{\mathrm{phys},d/m} = \frac{1}{\beta^2} \sum_{kk'} \chi_{d/m}^{qkk'}$. However, a susceptibility constructed this way contains divergences stemming from the mean-field phase transitions in DMFT, which largely overestimates critical temperatures [104]. This is even more true in two dimensions where the Mermin-Wagner theorem holds [105]. We remedy this artifact by employing a regularization parameter λ [33,34] (instead of doing fully fledged parquet [58] or self-consistent DΓA [61]). Here, λ is fixed by enforcing the sum rule

$$\frac{1}{2\beta} \sum_q \left(\chi_m^{q,\lambda_m} + \chi_d^{q,\lambda_d}\right) = \frac{n}{2}\left(1 - \frac{n}{2}\right), \tag{A7}$$

and $\chi_{d/m}^{q,\lambda} = [(\chi_{d/m}^q)^{-1} + \lambda_{d/m}]^{-1}$ is the λ-corrected susceptibility. Physically, $\lambda_{d/m}$ acts like an enhancement of the mass of the charge/spin fluctuations (or a reduction of the correlation length). The λ correction can dramatically change the susceptibility and suppress antiferromagnetic fluctuations. It does not, however, change the maximum of $\chi_{d/m}^q$. Hence, the spin dispersion in λ-corrected DΓA is the same as in DMFT.

[1] J. G. Bednorz and K. A. Müller, Z. Phys. B **64**, 189 (1986).
[2] D. Li, K. Lee, B. Y. Wang, M. Osada, S. Crossley, H. R. Lee, Y. Cui, Y. Hikita, and H. Y. Hwang, Nature (London) **572**, 624 (2019).
[3] D. Li, B. Y. Wang, K. Lee, S. P. Harvey, M. Osada, B. H. Goodge, L. F. Kourkoutis, and H. Y. Hwang, Phys. Rev. Lett. **125**, 027001 (2020).
[4] S. Zeng, C. S. Tang, X. Yin, C. Li, M. Li, Z. Huang, J. Hu, W. Liu, G. J. Omar, H. Jani, Z. S. Lim, K. Han, D. Wan, P. Yang, S. J. Pennycook, A. T. S. Wee, and A. Ariando, Phys. Rev. Lett. **125**, 147003 (2020).
[5] M. Osada, B. Y. Wang, K. Lee, D. Li, and H. Y. Hwang, Phys. Rev. Mater. **4**, 121801(R) (2020).
[6] S. Zeng, C. Li, L. Chow, Y. Cao, Z. Zhang, C. Tang, X. Yin, Z. Lim, J. Hu, P. Yang, and A. Ariando, Sci. Adv. **8**, eabl9927 (2022).
[7] G. A. Pan, D. F. Segedin, H. LaBollita, Q. Song, E. M. Nica, B. H. Goodge, A. T. Pierce, S. Doyle, S. Novakov, D. C. Carrizales, A. T. N'Diaye, P. Shafer, H. Paik, J. T. Heron, J. A. Mason, A. Yacoby, L. F. Kourkoutis, O. Erten, C. M. Brooks, A. S. Botana *et al.*, Nat. Mater. **21**, 160 (2022).
[8] M. Osada, B. Y. Wang, B. H. Goodge, S. P. Harvey, K. Lee, D. Li, L. F. Kourkoutis, and H. Y. Hwang, Adv. Mater. **33**, 2104083 (2021).
[9] N. N. Wang, M. W. Yang, Z. Yang, K. Y. Chen, H. Zhang, Q. H. Zhang, Z. H. Zhu, Y. Uwatoko, L. Gu, X. L. Dong, J. P. Sun, K. J. Jin, and J.-G. Cheng, Nat. Commun. **13**, 4367 (2022).
[10] J. Zaanen, G. A. Sawatzky, and J. W. Allen, Phys. Rev. Lett. **55**, 418 (1985).
[11] V. J. Emery, Phys. Rev. Lett. **58**, 2794 (1987).
[12] A. S. Botana and M. R. Norman, Phys. Rev. X **10**, 011024 (2020).
[13] H. Sakakibara, H. Usui, K. Suzuki, T. Kotani, H. Aoki, and K. Kuroki, Phys. Rev. Lett. **125**, 077003 (2020).
[14] P. Jiang, L. Si, Z. Liao, and Z. Zhong, Phys. Rev. B **100**, 201106(R) (2019).
[15] M. Hirayama, T. Tadano, Y. Nomura, and R. Arita, Phys. Rev. B **101**, 075107 (2020).
[16] L.-H. Hu and C. Wu, Phys. Rev. Res. **1**, 032046(R) (2019).
[17] X. Wu, D. Di Sante, T. Schwemmer, W. Hanke, H. Y. Hwang, S. Raghu, and R. Thomale, Phys. Rev. B **101**, 060504(R) (2020).
[18] Y. Nomura, M. Hirayama, T. Tadano, Y. Yoshimoto, K. Nakamura, and R. Arita, Phys. Rev. B **100**, 205138 (2019).
[19] G.-M. Zhang, Y.-F. Yang, and F.-C. Zhang, Phys. Rev. B **101**, 020501(R) (2020).
[20] M. Jiang, M. Berciu, and G. A. Sawatzky, Phys. Rev. Lett. **124**, 207004 (2020).
[21] P. Werner and S. Hoshino, Phys. Rev. B **101**, 041104(R) (2020).
[22] L. Si, W. Xiao, J. Kaufmann, J. M. Tomczak, Y. Lu, Z. Zhong, and K. Held, Phys. Rev. Lett. **124**, 166402 (2020).
[23] Y. Nomura and R. Arita, Rep. Prog. Phys. **85**, 052501 (2022).
[24] M. Kitatani, L. Si, P. Worm, J. M. Tomczak, R. Arita, and K. Held, Phys. Rev. Lett. **130**, 166002 (2023).
[25] M. Kitatani, L. Si, O. Janson, R. Arita, Z. Zhong, and K. Held, npj Quantum Mater. **5**, 59 (2020).
[26] K. Held, L. Si, P. Worm, O. Janson, R. Arita, Z. Zhong, J. M. Tomczak, and M. Kitatani, Front. Phys. **9**, 810394 (2022).
[27] This pocket also vanishes when going from infinite- to finite-layer nickelates [38].
[28] At larger doping, outside the superconducting dome, the Ni $3d_{z^2}$ band crosses the Fermi level in DFT+DMFT [25] and becomes relevant as well. Because of Hund's exchange this orbital cannot be treated as decoupled from the Ni $3d_{x^2-y^2}$ band. A similar picture has also been observed in other DFT+DMFT calculations [29,31]. In GW + DMFT the Ni $3d_{z^2}$ band touches the Fermi level already at lower dopings at large k_z [97], and in self-interaction corrected DFT+DMFT the Ni $3d_{z^2}$ band is even more prominent [96,103].
[29] J. Karp, A. S. Botana, M. R. Norman, H. Park, M. Zingl, and A. Millis, Phys. Rev. X **10**, 021061 (2020).
[30] J. Karp, A. Hampel, and A. J. Millis, Phys. Rev. B **105**, 205131 (2022).
[31] G. Pascut, L. Cosovanu, K. Haule, and K. F. Quader, Commun. Phys. **6**, 45 (2023).
[32] A. Toschi, A. A. Katanin, and K. Held, Phys. Rev. B **75**, 045118 (2007).

[33] A. A. Katanin, A. Toschi, and K. Held, Phys. Rev. B **80**, 075104 (2009).

[34] G. Rohringer, H. Hafermann, A. Toschi, A. A. Katanin, A. E. Antipov, M. I. Katsnelson, A. I. Lichtenstein, A. N. Rubtsov, and K. Held, Rev. Mod. Phys. **90**, 025003 (2018).

[35] M. Kitatani, R. Arita, T. Schäfer, and K. Held, J. Phys. Mater. **5**, 034005 (2022).

[36] K. Lee, B. Y. Wang, M. Osada, B. H. Goodge, T. C. Wang, Y. Lee, S. Harvey, W. J. Kim, Y. Yu, C. Murthy, S. Raghu, L. F. Kourkoutis, and H. Y. Hwang, Nature (London) **619**, 288 (2023).

[37] Note that the different substrate LSAT instead of STO [36] mainly allows for defect-free nickelate films, as is also obvious from the largely reduced resistivity. The change in lattice parameters is of minor importance; cf. the discussion in Sec. IV B.

[38] P. Worm, L. Si, M. Kitatani, R. Arita, J. M. Tomczak, and K. Held, Phys. Rev. Mater. **6**, L091801 (2022).

[39] H. Lu, M. Rossi, A. Nag, M. Osada, D. F. Li, K. Lee, B. Y. Wang, M. Garcia-Fernandez, S. Agrestini, Z. X. Shen, E. M. Been, B. Moritz, T. P. Devereaux, J. Zaanen, H. Y. Hwang, K.-J. Zhou, and W. S. Lee, Science **373**, 213 (2021).

[40] Y. Cui, C. Li, Q. Li, X. Zhu, Z. Hu, Y.-F. Yang, J. Zhang, R. Yu, H.-H. Wen, and W. Yu, Chin. Phys. Lett. **38**, 067401 (2021).

[41] J. Fowlie, M. Hadjimichael, M. M. Martins, D. Li, M. Osada, B. Y. Wang, K. Lee, Y. Lee, Z. Salman, T. Prokscha *et al.*, Nat. Phys. **18**, 1043 (2022).

[42] H. Lin, D. J. Gawryluk, Y. M. Klein, S. Huangfu, E. Pomjakushina, F. von Rohr, and A. Schilling, New J. Phys. **24**, 013022 (2022).

[43] R. A. Ortiz, P. Puphal, M. Klett, F. Hotz, R. K. Kremer, H. Trepka, M. Hemmida, H.-A. K. von Nidda, M. Isobe, R. Khasanov, H. Luetkens, P. Hansmann, B. Keimer, T. Schäfer, and M. Hepting, Phys. Rev. Res. **4**, 023093 (2022).

[44] M. Oda, N. Momono, and M. Ido, J. Phys. Chem. Solids **65**, 1381 (2004).

[45] B. Keimer, S. A. Kivelson, M. R. Norman, S. Uchida, and J. Zaanen, Nature (London) **518**, 179 (2015).

[46] Y. Nomura, T. Nomoto, M. Hirayama, and R. Arita, Phys. Rev. Res. **2**, 043144 (2020).

[47] M. Kitatani, Y. Nomura, M. Hirayama, and R. Arita, APL Mater. **11**, 030701 (2023).

[48] J. Hubbard, Proc. R. Soc. London, Ser. A **276**, 238 (1963).

[49] G. Kresse and J. Hafner, Phys. Rev. B **48**, 13115 (1993).

[50] J. P. Perdew, K. Burke, and M. Ernzerhof, Phys. Rev. Lett. **77**, 3865 (1996).

[51] P. Blaha, K. Schwarz, G. Madsen, D. Kvasnicka, J. Luitz, R. Laskowsk, F. Tran, L. Marks, and L. Marks, *Wien2k: An Augmented Plane Wave plus Local Orbitals Program for Calculating Crystal Properties* (TU Wien, Austria, 2019).

[52] K. Schwarz, P. Blaha, and G. K. H. Madsen, Comput. Phys. Commun. **147**, 71 (2002).

[53] J. Kuneš, R. Arita, P. Wissgott, A. Toschi, H. Ikeda, and K. Held, Comput. Phys. Commun. **181**, 1888 (2010).

[54] N. Marzari, A. A. Mostofi, J. R. Yates, I. Souza, and D. Vanderbilt, Rev. Mod. Phys. **84**, 1419 (2012).

[55] M. Casula, P. Werner, L. Vaugier, F. Aryasetiawan, T. Miyake, A. J. Millis, and S. Biermann, Phys. Rev. Lett. **109**, 126408 (2012).

[56] Q. Han, B. Chakrabarti, and K. Haule, arXiv:1810.06116.

[57] C. Honerkamp, H. Shinaoka, F. F. Assaad, and P. Werner, Phys. Rev. B **98**, 235151 (2018).

[58] A. Valli, T. Schäfer, P. Thunström, G. Rohringer, S. Andergassen, G. Sangiovanni, K. Held, and A. Toschi, Phys. Rev. B **91**, 115115 (2015).

[59] K. Held, in *Dynamical Mean-Field Theory of Correlated Electrons* (Forschungszentrum Jülich, 2022), Chap. Beyond DMFT: Spin fluctuations, pseudogaps and superconductivity, edited by E. Pavarini, E. Koch, D. Vollhardt, and A. I. Lichtenstein. Also available as arXiv:2208.03174.

[60] T. Schäfer, N. Wentzell, F. Šimkovic, Y.-Y. He, C. Hille, M. Klett, C. J. Eckhardt, B. Arzhang, V. Harkov, F.-M. Le Régent, A. Kirsch, Y. Wang, A. J. Kim, E. Kozik, E. A. Stepanov, A. Kauch, S. Andergassen, P. Hansmann, D. Rohe, Y. M. Vilk *et al.*, Phys. Rev. X **11**, 011058 (2021).

[61] J. Kaufmann, C. Eckhardt, M. Pickem, M. Kitatani, A. Kauch, and K. Held, Phys. Rev. B **103**, 035120 (2021).

[62] M. Wallerberger, A. Hausoel, P. Gunacker, A. Kowalski, N. Parragh, F. Goth, K. Held, and G. Sangiovanni, Comput. Phys. Commun. **235**, 388 (2019).

[63] P. Gunacker, M. Wallerberger, E. Gull, A. Hausoel, G. Sangiovanni, and K. Held, Phys. Rev. B **92**, 155102 (2015).

[64] P. Worm, DGApy (2023), doi: 10.5281/zenodo.10406493.

[65] P. Worm, Ph.D. thesis, TU Wien, 2023.

[66] J. Kaufmann and K. Held, Comput. Phys. Commun. **282**, 108519 (2023).

[67] J. E. Gubernatis, M. Jarrell, R. N. Silver, and D. S. Sivia, Phys. Rev. B **44**, 6011 (1991).

[68] G. J. Kraberger, R. Triebl, M. Zingl, and M. Aichhorn, Phys. Rev. B **96**, 155128 (2017).

[69] L. J. P. Ament, M. van Veenendaal, T. P. Devereaux, J. P. Hill, and J. van den Brink, Rev. Mod. Phys. **83**, 705 (2011).

[70] As for the dispersion, we plot the fitted damped harmonic oscillator, which is used as a model to describe the (para)magnon. The fit was performed by us as described by the authors of Ref. [39] in their supplemental material.

[71] Except for the magnitude, which has been adjusted in both experiments and in theory to a similar scale.

[72] See supplemental material of Ref. [39], Fig. S6(b).

[73] J.-Y. P. Delannoy, M. J. P. Gingras, P. C. W. Holdsworth, and A.-M. S. Tremblay, Phys. Rev. B **79**, 235130 (2009).

[74] R. Coldea, S. M. Hayden, G. Aeppli, T. G. Perring, C. D. Frost, T. E. Mason, S.-W. Cheong, and Z. Fisk, Phys. Rev. Lett. **86**, 5377 (2001).

[75] O. Ivashko, M. Horio, W. Wan, N. B. Christensen, D. E. McNally, E. Paris, Y. Tseng, N. E. Shaik, H. M. Rønnow, H. I. Wei, C. Adamo, C. Lichtensteiger, M. Gibert, M. R. Beasley, K. M. Shen, J. M. Tomczak, T. Schmitt, and J. Chang, Nat. Commun. **10**, 786 (2019).

[76] I. Biało, L. Martinelli, G. De Luca, P. Worm, A. Drewanowski, J. Choi, M. Garcia-Fernandez, S. Agrestini, K.-J. Zhou, L. Guo, C. B. Eom, J. M. Tomczak, K. Held, M. Gibert, Q. Wang, and J. Chang, arXiv:2306.05828.

[77] $U = 9t$ has been considered in Ref. [25] to be the maximal U still consistent with the cRPA, while $U = 8t$ is the best estimate.

[78] A dependence of T_c on the residual resistivity, which was taken as a proxy measure for disorder and lattice defects, was also reported in Ref. [106] and cleaner films show a larger T_c in a manner "not too different from cuprate superconductors."

Indeed, cuprates show a decrease in T_c for an increasing in-plane [107], out-of-plane [108–110] resistivity and when magnetic or nonmagnetic impurities are introduced [111].

[79] It is common practice to use La instead of Nd to avoid the (wrong) appearance of f bands around the Fermi energy. For treating Nd directly the Nd f-shell electrons are usually considered as core electrons.

[80] About ∼4% because of a change in t and another 5%–10% because of the change in U/t.

[81] Larger changes of the hopping parameters are possible by applying pressure; see Ref. [112].

[82] Effects beyond the single-band model will always lead to some discrepancy. For this reason, we refrain from fine-tuning parameters.

[83] Q. Gao, S. Fan, Q. Wang, J. Li, X. Ren, I. Bialo, A. Drewanowski, P. Rothenbühler, J. Choi, Y. Wang, T. Xiang, J. Hu, K.-J. Zhou, V. Bisogni, R. Comin, J. Chang, J. Pelliciari, X. J. Zhou, and Z. Zhu, arXiv:2208.05614.

[84] L. Wang, G. He, Z. Yang, M. Garcia-Fernandez, A. Nag, K. Zhou, M. Minola, M. L. Tacon, B. Keimer, Y. Peng, and Y. Li, Nat. Commun. **13**, 3163 (2022).

[85] See for examples Fig. 1 in Ref. [36].

[86] O. J. Lipscombe, B. Vignolle, T. G. Perring, C. D. Frost, and S. M. Hayden, Phys. Rev. Lett. **102**, 167002 (2009).

[87] M. Fujita, H. Hiraka, M. Matsuda, M. Matsuura, J. M. Tranquada, S. Wakimoto, G. Xu, and K. Yamada, J. Phys. Soc. Jpn. **81**, 011007 (2012).

[88] Let us note that the prototypical cuprate L_2CuO_4 is a 214 layered system compared to the 112 layer structure of nickelates.

[89] Q. Gu, Y. Li, S. Wan, H. Li, W. Guo, H. Yang, Q. Li, X. Zhu, X. Pan, Y. Nie, and H.-H. Wen, Nat. Commun. **11**, 6027 (2020).

[90] S. P. Harvey, B. Y. Wang, J. Fowlie, M. Osada, K. Lee, Y. Lee, D. Li, and H. Y. Hwang, arXiv:2201.12971.

[91] L. E. Chow, S. K. Sudheesh, P. Nandi, S. W. Zeng, Z. T. Zhang, X. M. Du, Z. S. Lim, E. E. M. Chia, and A. Ariando, arXiv:2201.10038.

[92] P. A. Lee, N. Nagaosa, and X.-G. Wen, Rev. Mod. Phys. **78**, 17 (2006).

[93] D. J. Scalapino, Rev. Mod. Phys. **84**, 1383 (2012).

[94] E. Fradkin, S. A. Kivelson, and J. M. Tranquada, Rev. Mod. Phys. **87**, 457 (2015).

[95] Cf. Refs. [113] and [114] for an in-depth analysis of the pairing vertex in the Hubbard model and its fluctuation diagnostic [115].

[96] A. Kreisel, B. M. Andersen, A. T. Rømer, I. M. Eremin, and F. Lechermann, Phys. Rev. Lett. **129**, 077002 (2022).

[97] F. Petocchi, V. Christiansson, F. Nilsson, F. Aryasetiawan, and P. Werner, Phys. Rev. X **10**, 041047 (2020).

[98] Y.-f. Yang and G.-M. Zhang, Front. Phys. **9**, 801236 (2022).

[99] A. A. C. Alvarez, L. Iglesias, S. Petit, W. Prellier, M. Bibes, and J. Varignon, arXiv:2211.04870.

[100] Y.-T. Tseng, M. O. Malcolms, H. Menke, M. Klett, T. Schäfer, and P. Hansmann, arXiv:2311.09023.

[101] X. Ding, Y. Fan, X. X. Wang, C. H. Li, Z. T. An, J. H. Ye, S. L. Tang, M. Y. N. Lei, X. T. Sun, N. Guo, Z. H. Chen, S. Sangphet, Y. L. Wang, H. C. Xu, R. Peng, and D. L. Feng, arXiv:2403.07448.

[102] W. Sun, Z. Jiang, C. Xia, B. Hao, Y. Li, S. Yan, M. Wang, H. Liu, J. Ding, J. Liu, Z. Liu, J. Liu, H. Chen, D. Shen, and Y. Nie, arXiv:2403.07344.

[103] F. Lechermann, Phys. Rev. B **101**, 081110(R) (2020).

[104] G. Rohringer, A. Toschi, A. Katanin, and K. Held, Phys. Rev. Lett. **107**, 256402 (2011).

[105] N. D. Mermin and H. Wagner, Phys. Rev. Lett. **17**, 1307 (1966).

[106] Y.-T. Hsu, M. Osada, B. Y. Wang, M. Berben, C. Duffy, S. P. Harvey, K. Lee, D. Li, S. Wiedmann, H. Y. Hwang, and N. E. Hussey, Front. Phys. **10**, 846639 (2022).

[107] Y. Fukuzumi, K. Mizuhashi, K. Takenaka, and S. Uchida, Phys. Rev. Lett. **76**, 684 (1996).

[108] H. Hobou, S. Ishida, K. Fujita, M. Ishikado, K. M. Kojima, H. Eisaki, and S. Uchida, Phys. Rev. B **79**, 064507 (2009).

[109] H. Eisaki, N. Kaneko, D. L. Feng, A. Damascelli, P. K. Mang, K. M. Shen, Z.-X. Shen, and M. Greven, Phys. Rev. B **69**, 064512 (2004).

[110] K. Fujita, T. Noda, K. M. Kojima, H. Eisaki, and S. Uchida, Phys. Rev. Lett. **95**, 097006 (2005).

[111] D. A. Bonn, S. Kamal, K. Zhang, R. Liang, D. J. Baar, E. Klein, and W. N. Hardy, Phys. Rev. B **50**, 4051 (1994).

[112] S. Di Cataldo, P. Worm, J. Tomczak, L. Si, and K. Held, Nat. Commun. **15**, 3952 (2024).

[113] M. Kitatani, T. Schäfer, H. Aoki, and K. Held, Phys. Rev. B **99**, 041115(R) (2019).

[114] X. Dong, L. D. Re, A. Toschi, and E. Gull, Proc. Natl. Acad. Sci. U.S.A. **119**, e2205048119 (2022).

[115] T. Schäfer and A. Toschi, J. Phys.: Condens. Matter **33**, 214001 (2021).